remote sensing

MDPI

Article

A New Algorithm for the Global-Scale Quantification of Volcanic SO_2 Exploiting the Sentinel-5P TROPOMI and Google Earth Engine

Maddalena Dozzo [1,2], Alessandro Aiuppa [2], Giuseppe Bilotta [1], Annalisa Cappello [1] and Gaetana Ganci [1,*]

[1] Istituto Nazionale di Geofisica e Vulcanologia, OE, 95125 Catania, CT, Italy; maddalena.dozzo@ingv.it (M.D.); giuseppe.bilotta@ingv.it (G.B.); annalisa.cappello@ingv.it (A.C.)
[2] Dipartimento di Scienze della Terra e del Mare (DiSTeM), Università degli Studi di Palermo, 90123 Palermo, PA, Italy; alessandro.aiuppa@unipa.it
* Correspondence: gaetana.ganci@ingv.it

Abstract: Sulfur dioxide (SO_2) is sourced by degassing magma in the shallow crust; hence its monitoring provides information on the rates of magma ascent in the feeding conduit and the style and intensity of eruption, ultimately contributing to volcano monitoring and hazard assessment. Here, we present a new algorithm to extract SO_2 data from the TROPOMI imaging spectrometer aboard the Sentinel-5 Precursor satellite, which delivers atmospheric column measurements of sulfur dioxide and other gases with an unprecedented spatial resolution and daily revisit time. Specifically, we automatically extract the volcanic clouds by introducing a two-step approach. Firstly, we used the Simple Non-Iterative Clustering segmentation method, which is an object-based image analysis approach; secondly, the K-means unsupervised machine learning technique is applied to the segmented images, allowing a further and better clustering to distinguish the SO_2. We implemented this algorithm in the open-source Google Earth Engine computing platform, which provides TROPOMI imagery collection adjusted in terms of quality parameters. As case studies, we chose three volcanoes: Mount Etna (Italy), Taal (Philippines) and Sangay (Ecuador); we calculated sulfur dioxide mass values from 2018 to date, focusing on a few paroxysmal events. Our results are compared with data available in the literature and with Level 2 TROPOMI imagery, where a mask is provided to identify SO_2, finding an optimal agreement. This work paves the way to the release of SO_2 flux time series with reduced delay and improved calculation time, hence contributing to a rapid response to volcanic unrest/eruption at volcanoes worldwide.

Keywords: clustering analysis; Google Earth Engine; K-means algorithm; Sentinel-5P; sulfur dioxide; volcanic eruption

Academic Editor: Gianluca Groppelli

Received: 15 November 2024
Revised: 15 January 2025
Accepted: 27 January 2025
Published: 5 February 2025

Citation: Dozzo, M.; Aiuppa, A.; Bilotta, G.; Cappello, A.; Ganci, G. A New Algorithm for the Global-Scale Quantification of Volcanic SO_2 Exploiting the Sentinel-5P TROPOMI and Google Earth Engine. *Remote Sens.* **2025**, *17*, 534. https://doi.org/10.3390/rs17030534

1. Introduction

Sulfur dioxide (SO_2) is released into the atmosphere both from anthropogenic and natural (mainly volcanic) activities [1,2], altering air quality [3–6], local ecosystems [7–10] and affecting human and animal health [11–13].

Anthropogenic SO_2 may result from coal-burning power plants, oil refineries and smelters [14,15], whereas volcanic sulfur dioxide is emitted from the degassing of magma in the mid/upper crust and represents the most abundant gas, after water vapor and carbon dioxide [2,16,17].

The injection of SO_2 into the upper-troposphere and lower-stratosphere can also lead to significant changes in the global climate, since this gas rapidly oxidizes into sulfuric

acid and sulfate aerosols, with a subsequent general lowering of temperatures in the years following an eruption [18–22].

Sulfur dioxide is released from magma at relatively shallow depth, making it the most suitable gas for monitoring volcanic activity dynamics through remote sensing techniques. Measuring volcanic SO_2 flux is of vital importance for volcano monitoring, understanding the processes that may lead to an eruption [2,17] and tracking the progression of an ongoing eruption [23], either as a proxy for the eruption rate [24] or evaluating the endogenous growth of a lava flow field [25]. SO_2 mass fluxes reflect the dynamics of the magma and the processes of decompression and crystallization, providing information on the depth of gas–magma separation, on the structure of the conduit and on the permeability and pressure of the magma, as well as on the eruptive style and explosiveness [17,26–31].

SO_2 can also be considered a proxy for magma effusive rate when thermal anomalies are not quantifiable because they are covered by the volcanic plume [32]. Therefore, the estimation of SO_2 emissions can play a crucial role in volcanic monitoring to evaluate hazards and mitigate the associated risk.

SO_2 emissions can be monitored from the ground using networks of UV-DOAS instruments installed close to volcanic sources, e.g., [33]. However, only a small number of active volcanoes are equipped with ground monitoring systems, primarily due to limited resources [34]. Additionally, the perspective from ground-based instruments provides a restricted view of the plume. As a result, during heightened volcanic activity, ground sensors may become less reliable or fail altogether, especially near the source where a high concentration of ash and aerosols can obscure the plume, e.g., [35,36]. In this regard, satellites represent a helpful tool to monitor global SO_2 emissions and assess their environmental impacts. Sulfur dioxide is estimated from satellites using Vertical Column Densities (VCDs), which represent the total number of molecules in a vertical column per unit area. The most widespread algorithm for obtaining VCDs is based on the differential optical absorption spectroscopy (DOAS; [37]) technique, in which a spectral analysis provides the densities of the inclined column of SO_2 (or other gases) (SCDs), corrected through an empirical method to then be converted into vertical column densities through the radiative transfer calculation of Air Mass Factors (AMFs).

Since the late nineteen-seventies, due to its strong absorption of UV radiation, SO_2 VCDs have been provided by several ultraviolet (UV) polar-orbiting nadir instruments, namely, the Total Ozone Monitoring Spectrometer (TOMS; [38]), Global Ozone Monitoring Experiment (GOME; [39,40]), SCanning Imaging Absorption spectroMeter for Atmospheric CHartographY (SCIAMACHY; [41–43]), Ozone Monitoring Instrument (OMI; [44–47]), Global Ozone Monitoring Experiment-2 (GOME-2; [48–50]), Ozone Mapping and Profiler Suite (OMPS; [51,52]) and TROPOspheric Monitoring Instrument (TROPOMI; [53]).

Satellite SO_2 measurements with sufficient spatial resolution to detect hundreds of SO_2 emission sources began with the OMI instrument on NASA's Earth Observing System (EOS) Aura spacecraft [54] in 2004. OMI offers a spatial resolution of 13 km $\times$ 24 km at nadir and can generate daily, nearly global maps of SO_2 VCDs [46,55]. The most recent instrument (TROPOMI), launched in 2017 on the ESA Copernicus Sentinel-5 Precursor spacecraft [56], provides the highest spatial resolution (5.5 km $\times$ 3.5 km at nadir) among all hyperspectral sensors and is capable of delivering daily near-global coverage [57,58].

Since the launch of the Sentinel-5P satellite in October 2017, several applications have been made for monitoring volcanic gases (e.g., [53,59–69]). These studies have, for example, exploited the retrieved vertical column density (VCD) of SO_2 to generate time–flux series for both short- and long-term degassing and explosive events [53,62,63,66–69] or assimilated SO_2 retrieval to plume trajectory forecasting [61]. A few attempts have been also made to

apply Artificial Intelligence to the automatic detection of SO_2 [70] or to retrieve the volcanic source from the plume shape where different volcanoes exist [71].

Here, we present a new method to calculate SO_2 mass, exploiting Artificial Intelligence (AI) and the open-source Google Earth Engine (GEE) cloud computing platform, which uses a JavaScript programming language and contains the collection of TROPOMI imagery from 2018 to date, with a global coverage. We developed a programming code to rapidly and automatically extrapolate this information, exploiting the combination of segmentation and clustering techniques, which allow us to obtain a result in a short time and which is applicable on a global scale.

The benefit of using GEE is closely connected to the possibility of managing a huge amount of data, obtaining a result in a very short time. Indeed, different from the classic uses of TROPOMI data, it is not necessary here to carry out time-consuming procedures, such as the download of the data and the subsequent pre-processing to check their quality.

GEE provides a gridded Level 3 (L3) TROPOMI product, available only in this platform and created by aggregating and interpolating geophysical parameters from Level 2 (L2) data onto a regular spatio-temporal grid, which ensures uniform spacing. This last product is derived directly from the raw measurements (Level 0 data), which are calibrated and georeferenced. The rationale for our method arises from the fact that a mask for the detection of sulfur dioxide is lacking in the L3; moreover, the calculation of the total mass of SO_2 by applying a simple fixed threshold directly to the TROPOMI L3 product does not allow obtaining optimal results for different cases [72].

To demonstrate our approach, we report a few examples where the total SO_2 VCD data were calculated on three open-vent volcanoes and compared with results obtained using the detection mask in the Level 2 (L2) TROPOMI product. In particular, we analyze (i) different paroxysmal events occurring at Mount Etna, one of the most active volcanoes in the world [1,26,73], typically emitting from the summit open vents 500 to 5000 tons of sulfur dioxide/daily and for which a lot of ground and satellite data are available for comparison; (ii) the explosive activity of Taal volcano (Philippines), one of the most dangerous active volcanoes in the world, which has produced thirty-four historical eruptions over the last two centuries [74,75] and (iii) a few of the strongest eruptive events occurring at Sangay, located in the southwest part of Ecuador [76–78].

2. Materials and Methods

Sentinel-5P is a sun-synchronous, quasi-polar satellite in low-Earth orbit at an altitude of 824 km (824 km) that provides near-complete daily coverage of the Earth's surface. It has a swath of 2600 km and an orbital cycle lasting 16 days, completing 14 orbits per day and approximately 227 orbits per cycle. The TROPOMI instrument onboard collects data across four spectral regions (ultraviolet, visible, near and short-wave infrared), enabling the detection of SO_2 along with several other gases (O_3, NO_2, CO, CH_4, and HCHO) and aerosols [56]. The sensor's pixel size near the nadir was 3.5 km (across-track) $\times$ 7 km (along-track) for data acquired up to August 2019, which improved to 3.5 km $\times$ 5.5 km for more recent images [79]. This satellite employs passive remote sensing techniques to achieve its objective by measuring the solar radiation reflected by and emitted from the Earth at the Top Of Atmosphere (TOA). The GEE platform provides two different Level 3 TROPOMI products, namely Sentinel-5P Offline Sulfur Dioxide (OFFL) and Sentinel-5P Near-Real-Time Sulfur Dioxide (NRTI). This second product is designed for near-real-time applications and remains available for 15-days after acquisition, after which it is merged into and replaced by the OFFL product.

To obtain the Level 3 product, the original Sentinel-5P Level 2 data from the European Space Agency is re-gridded and merged. The software package HARP (Harmonized

Access to Remote Data for Processing) is used to merge and re-grid the data in order to keep a single grid per orbit. HARP applies the "bin_spatial" operation, which spatially averages pixel values between overlapping scenes for a given day of collection, effectively combining multiple scenes into a single, consistent spatial grid. This ensures that the data is harmonized into a global grid with a uniform spatial resolution. In addition to spatial regridding, HARP performs data filtering based on quality assurance (QA) parameters. The filtering process evaluates several factors, such as the presence of clouds, snow, or ice on the surface, and removes low-quality pixels to enhance the reliability of the final dataset. Specific filtering criteria are applied depending on the atmospheric product, ensuring that only high-confidence observations contribute to the Level 3 output. After the data is harmonized using HARP, OptimizeRasters, a tool designed to streamline large geospatial datasets, is used to convert the processed data into a Cloud Optimized GeoTIFF (COG) format. The COG format enhances accessibility and performance for cloud-based applications, making the Level 3 product suitable for rapid retrieval and analysis. This process results in a high-resolution dataset with a native spatial resolution of approximately $0.1^\circ \times 0.1^\circ$ (https://www.arcgis.com/home/item.html?id=a55b4201015d426e845789b67ef1ab15, accessed on 1 September 2024). The Level 3 data are further refined through robust QA adjustments, taking into account multiple quality parameters. These adjustments include the exclusion of unreliable pixels caused by atmospheric obstructions, such as thick cloud cover, or challenging surface conditions, like snow and ice. The integration of these quality controls ensures that the final dataset provides accurate and reliable information for various applications in atmospheric science, environmental monitoring and policymaking. The correction is made to satisfy all the following criteria, as recommended by the Mission Performance Center experts, who are responsible for ensuring that the products derived from satellite data meet the required quality standards (this includes monitoring mission performance, instrument calibration, validation of scientific products and implementing corrections or improvements necessary to maintain data reliability), and by the Sentinel-5P Validation Team (https://sentinel.esa.int/documents/247904/3541451/Sentinel-5P-Sulphur-Dioxide-Readme.pdf, accessed on 1 September 2024):

-snow_ice < 0.5
-sulfurdioxide_total_air_mass_factor_polluted > 0.1
-sulfurdioxide_total_vertical_column > -0.001 mol/m^2
-qa_value > 0.5 (a continuous quality indicator ranging from 0, representing a processing error, to 1 (or 100%), which denotes optimal quality)
-cloud_fraction_crb < 0.3 (a dimensionless parameter representing the intensity-weighted cloud fraction, calculated as the ratio of vertical column densities in clear-sky versus clouding conditions, ranging from 0 for clear skies to 1 for fully cloudy conditions [51].
-solar_zenith_angle < 60°

Negative vertical column values are frequently observed in clean regions or areas with low SO_2 emissions due to data noise. It is recommended not to filter these values except for outliers, especially for vertical columns below -0.001 mol/m^2.

The methodology developed for processing Sentinel-5P TROPOMI imagery is illustrated in the flowchart of Figure 1.

For this study, we exploit the offline product, which is better than NRTI since it contains fewer data gaps and missing values thanks to the more thorough processing, which is particularly important for applications that require complete time series. The OFFL assets contain data from a single orbit (with data only for a single hemisphere due to half of the Earth being dark).

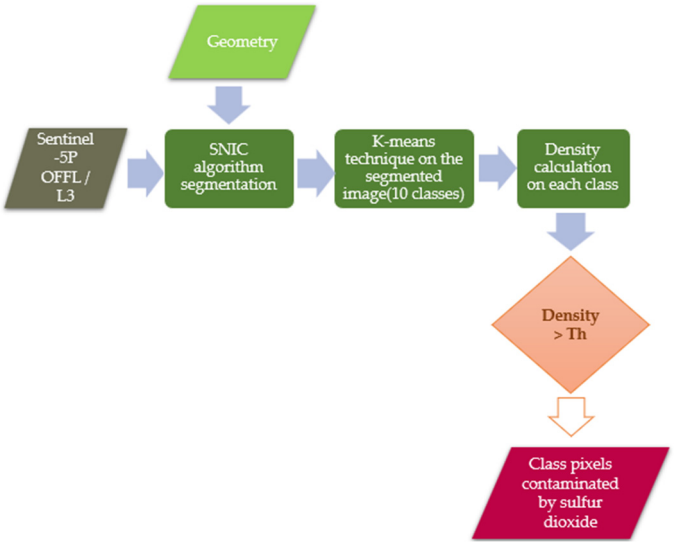

Figure 1. Flowchart with the main steps of the methodology: Sentinel-5P Offline/Level 3 Product PS imagery and the geometry outlined around the volcano represent the data input; dark green rectangles report the main processing steps (where GEE stands for Google Earth Engine and SNIC for Simple Non-Iterative Clustering), while the red parallelogram represents the output to highlight the pixels contaminated by SO_2 within those classes with a density higher than the selected threshold, Th.

GEE provides two different products for the calculation of the SO_2 vertical column density, which is calculated using the DOAS technique, retrieved assuming a plume center-of-mass at ground level and 15 km altitude. The layer at 7 km lacks here, not allowing us to interpolate to the "true" SO_2 plume height. In this regard, we exploited the product at 15 km (the "SO_2_column_number_density_15 km" on GEE), providing SO_2 integrated column density values in molar concentrations (mol/m^2), which can also be expressed in Dobson Units (DU), where 1 DU = 2.69 $\times$ 1016 molecules/cm^2, and indicate the number of SO_2 molecules in an atmospheric column per unit area. This product allowed us to study those eruptive events where the eruptive column reached several km above the vent.

To highlight those pixels contaminated by SO_2, avoiding the inclusion of noisy artifacts in the analysis, which show higher SO_2 VCD values than pixels actually within the plume, two different clustering techniques were applied to pixels contained within a geometry centered on the volcano that was large enough to include most of the volcanic plume. First, we applied to Sentinel-5P Offline Sulfur Dioxide image collection a Simple Non-Iterative Clustering (SNIC) algorithm segmentation and then a k-means unsupervised classifier, which therefore does not require data labeling. This two-step approach for object-based image analysis is meant to better characterize the sulfur dioxide, avoiding considering the noise that could derive, for example, from the sensor instrumentation onboard the satellites or from the light and atmospheric conditions [80].

Image segmentation is a technique that partitions an image into multiple segments. Research has shown that segmentation methods like Multi-Resolution Segmentation (MRS), Simple Linear Iterative Clustering (SLIC) and Simple Non-Iterative Clustering (SNIC) provide an innovative and evolving approach, particularly for high-resolution remote sensing images, surpassing traditional pixel-based classification methods [81–85]. Some recent studies have demonstrated how the combination of segmentation and classification techniques allows achieving higher accuracy than pixel-based classification algorithms, together with significantly reducing processing time [86]. Based on the segmentation outcomes, image segmentation can be categorized into two types, one focuses on delineating field boundaries [87,88], while the other simplifies the image into small clusters of connected pixels with similar properties, known as objects or superpixels [82,89,90]. Due

to its simplicity and efficiency, superpixel segmentation has garnered increased attention recently [83,84,91]. SNIC, an advanced superpixel segmentation algorithm developed from SLIC, offers benefits such as lower memory usage and higher processing speed since it is non-iterative. SNIC's effectiveness as a preprocessing algorithm is attributed to its simplicity, computational efficiency and its capability to produce superpixels that exhibit good boundary adherence and limited adjacency [89]. It has demonstrated significant potential in applications such as land use–land cover classification [92,93], hyperspectral data classification [94], crop mapping [95,96] and wetland inventory [97].

The SNIC algorithm begins by placing K initial centroids on a regular grid within the image plane. Each centroid is associated with an element that comprises spatial position, superpixel label and the distance from the superpixel centroid to the candidate pixel [94]. These elements are then added to a priority queue Q. The algorithm continuously processes the element with the smallest distance from the queue. For each neighboring pixel of the processed element, if the pixel has not been labeled, a new element is created with the distance and label of the connected centroid and then added to the queue. As new elements are added, the corresponding centroid values are updated in real time. The algorithm continues this process until all image pixels are labeled and the priority queue is empty, at which point the SNIC algorithm concludes [89]. SNIC identifies the objects (clusters) based on the specified input parameters and produces a multi-band raster. This raster includes the cluster assignments as well as additional layers containing the average values of the input features.

It requires setting some key parameters: the "compactness factor", which affects the shape of the clusters (larger values result in more compact clusters); the "connectivity" (having a value of 4 or 8), which refers to the internal cohesion of superpixels; and the "neighborhoodSize", namely the target dimension of each superpixel in terms of pixel number, which is relevant to avoid tile boundary artifacts. Changing each parameter individually is essential to be able to learn what characteristics of the SNIC clustering they control. To assign key parameters, we used a trial-and-error approach, a commonly accepted method for the SNIC [98,99], searching for values that are usually considered for this segmentation technique and adjusting them for our purpose on the basis of visual results inspection and the specific characteristics of the image (mainly the spatial resolution).

In our application, we set the compactness at 20, the connectivity at 4 and the neighborhood size at 20 (Figure 2), finding in these values the best configuration for our purpose. Indeed, regarding the compactness, a value of 20 is adapted to balance the compactness of the superpixels with the need to preserve image details. A value of 4 for the connectivity allows us to obtain a well-structured segmentation, being at the same time simpler and less computationally expensive than 8-connectivity.

Finally, we assigned 20 as the neighborhood size to avoid dividing the image into excessively small superpixels. It is worth noting that the key parameters for the SNIC algorithm were also based on the visual assessment of the k-means output, which varies greatly depending on the chosen values.

The k-means unsupervised machine learning technique was then applied on the segmented images to group all pixels of each cluster, defined as a single point, to have the same class. This allowed us to improve our classification, shifting from a pixel-based approach to one that reveals clear and distinct objects in the landscape. Indeed, applying the k-means on superpixels allows us to refine the segmentation, focusing on the internal details of the regions defined by SNIC. Moreover, preliminary segmentation with SNIC followed by k-means on superpixels makes imagery easier to process, reducing computational complexity, as the number of regions is reduced compared to the original image.

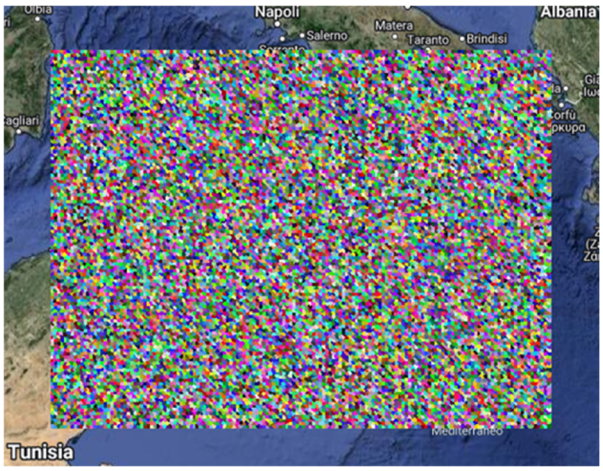

Figure 2. Example of the Simple Non-Iterative Clustering algorithm applied on the Sentinel-5P Offline SO_2 product of 2 June 2021 for Mt. Etna (Italy).

K-means is a numerical, unsupervised, non-deterministic, iterative method. Its simplicity and speed make it highly effective in many practical applications, often yielding good clustering results. The algorithm operates in two distinct phases. In the first phase, k centers are randomly initialized, with the value of k set by the user. In the subsequent phase, each data point is assigned to the nearest center, typically determined using the Euclidean distance [100]. Once all data objects are assigned to clusters, an initial grouping is formed and the average of these clusters is recalculated. This iterative process repeats until the criterion function reaches its minimum. The k-means clustering algorithm always converges to a local minimum. Before convergence, distance calculations and cluster center updates occur through several loop iterations, with the number of k-means iterations denoted by the positive integer t. The exact value of t depends on the initial positions of the cluster centers [101]. For our purposes, we chose a number of clusters (or classes) equal to 10, so as to obtain a detailed classification based on the SO_2 concentration. Figure 3 reports the Sentinel-5P TROPOMI product available on the Copernicus browser (https://browser.dataspace.copernicus.eu, accessed on 1 September 2024) for Mt. Etna for 2 June 2021 (characterized by a paroxysmal event) (Figure 3a), with the associated classification results after the application of the SNIC and k-means techniques (Figure 3b).

The volcanic plume is obtained by selecting the classes with a higher SO_2 density, defined as the ratio between the total mass value of SO_2 (given by the sum of the SO_2 values of each pixel for each class) and the relative number of pixels contained in each class. In this way, we were able to calculate the sulfur dioxide total mass value considering only the pixel within the volcanic plume. In particular, we considered a density threshold equal to 0.00028 mol/m^2, at which we found an optimal value for all the eruptive events analyzed to distinguish the pixels contaminated by SO_2; in this way, the plume consists of a few continuous classes.

The Level 3 TROPOMI product does not contain a mask for the identification of the pixels contaminated by the SO_2, which is available for the Level 2 product. In this regard, we exploited this product for a comparison, importing it into Matlab as a netCDF-4 format (.nc), which is freely obtained via the ESA-Copernicus Sentinel-5P Pre Operation Data-Hub and generated within the Copernicus ground system (https://sentinel.esa.int/documents/247904/3541451/Sentinel-5P-Sulphur-Dioxide-Readme.pdf (accessed on 1 September 2024)). L2 products are derived from Level 0 raw data that are calibrated and georeferenced and then processed to Level 1, including radiance and irradiance. Finally, L2 products containing SO_2 concentrations are extracted from the ultraviolet (UV) spectrum using algorithms based on differential optical absorption spectroscopy (DOAS), employing

a combination of three fitting windows: 312–326, 325–335 or 360–390 nm [51]. To select only pixels containing SO_2, users must filter pixels using "sulfurdioxide_detection_flag" > 0. This flag identifies pixels with a high SO_2 concentration [102], assigning values as follows: 0 for no detection, 1 for SO_2 detection, 2 for clear volcanic detection, 3 for detection close to a known anthropogenic source or 4 for detection at a high solar zenith angle, which may indicate a potential false positive. By summing the pixels of the volcanic SO_2 detection mask and using the vertical column density (in our case at 15 km), the total mass of volcanic SO_2 plumes in the image can be estimated [103].

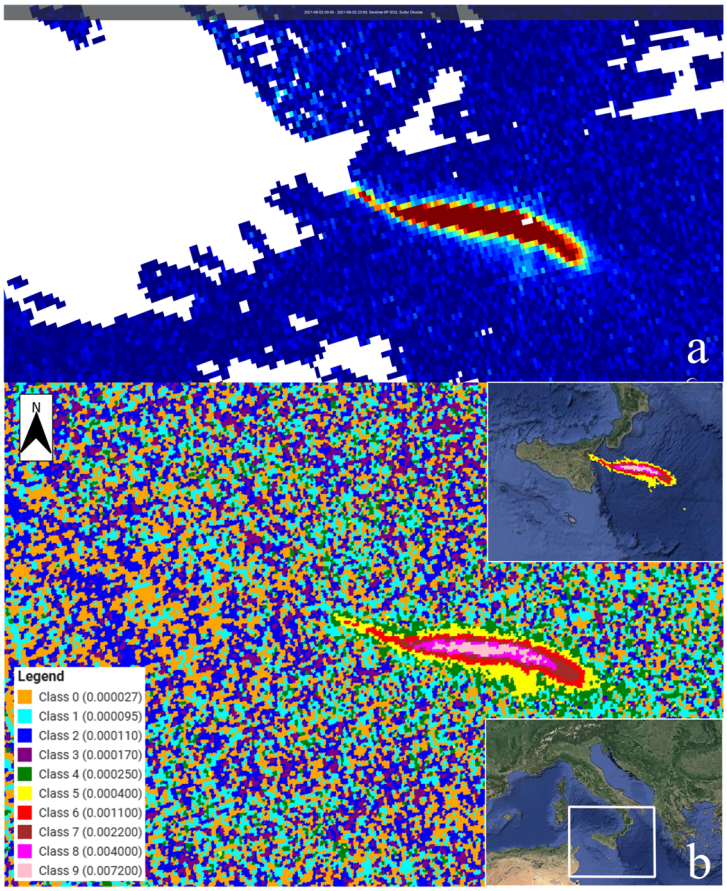

Figure 3. (**a**) Sentinel-5P TROPOMI product available on the Copernicus browser for Mt. Etna for 2 June 2021. (**b**) The same product after the application of the SNIC and k-means techniques, reporting in the legend the 10 classes (with the relative density values in brackets). In the top right inset the resulting plume is highlighted, while in the bottom right inset the map of Italy with the area considered for the calculation framed in white is reported.

In this work, we focused on three different volcanoes: Mt. Etna (Italy), Sangay (Ecuador) and Taal (Philippines). We analyzed four eruptive events for each volcano that occurred near the passage of the TROPOMI satellite and reached several km above the vent.

Mt. Etna consistently exhibits persistent degassing, primarily maintained by the passive release of gas from shallow convecting magma [26]. This typically includes mild intra-crater Strombolian explosive activity. However, this routine activity is often interrupted by effusive eruptions [104–107] and occasionally by violent paroxysmal explosive events [108]. For this volcano, we considered the paroxysmal events that occurred on 19 April 2020, 1 April 2021, 2 June 2021, and 20 July 2021.

Sangay is a strato-volcano located on the upper eastern flank of the Eastern Cordillera of Ecuador and is one of the most active volcanoes in the world, with nearly continuous activity since 1628 [109,110]. The volcano has been under instrumental monitoring by the

Instituto Geofísico of the Escuela Politécnica Nacional since 2013. In May 2019, the volcano entered a new eruptive phase, which has been classified as the most intense eruption in the last six decades [78]. However, ground-based monitoring at Sangay is limited due to its remote location, making access challenging and the installation of instruments extremely difficult. Additionally, real-time data transmission is only possible via satellite link. Due to these challenges, satellite-based monitoring of Sangay is crucial for hazard assessment. For this volcano, the eruptive events that occurred on 20 September 2020, 11 March 2021, 7 May 2021 and 16 May 2021 were considered.

Taal volcano, located in Batangas, is a caldera system and one of the most active volcanoes in the Philippines. It has experienced approximately 35 recorded eruptions since 3580 BCE, ranging from VEI 1 to 6, the majority being VEI 2. The caldera contains a lake with an island that also has a lake within the Main Crater. The first activity was registered in 1572. One of the most significant eruptions occurred on 12–13 January 2020, 43 years after its previous eruption in 1977, when the volcano spewed an ash column exceeding 1 km in thickness, then increasing in intensity and generating a 10–15 km tall steam-laden tephra column [111]. We took into account the eruptions that occurred at Taal volcano on 12–13 January 2020, 1 July 2021, 26 March 2022 and 12 April 2024.

3. Results

We report here the time series related to the total SO_2 mass for the three cases of study, showing a time window of one or two years for each volcano. In Figure 4 are reported the values, expressed in kilotons (kton), calculated for Mt. Etna from January 2020 to December 2021, in which the volcano produced several lava fountaining episodes.

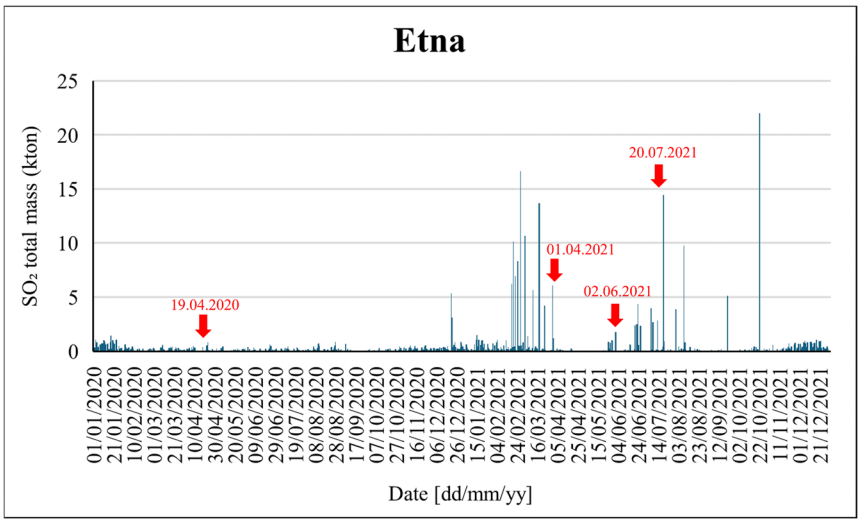

Figure 4. SO_2 total mass time series calculated for Mt. Etna, expressed in kton. The red arrows indicate the events analyzed in more detail.

Several peaks are visible, especially in 2021, when different paroxysmal events occurred sometimes many times a day, producing high eruptive columns and tons of SO_2, as reported in the INGV-OE bulletins (www.ct.ingv.it; accessed on 1 September 2024), where the SO_2 flux is measured by the ground-based FLAME network [112].

During the first months of 2020, the eruptive activity of Mt. Etna was sporadic, with a few strombolian episodes often associated with the highest values of SO_2 total mass. In the period between the beginning of April and the first half of May, many values around zero are visible in Figure 4, corresponding to a period of poor degassing for Mt. Etna. The activity resumed in August 2020, when two paroxysmal events occurred on 21 and 22 December 2020. The highest value in this time series corresponds to the event of 23 October

2021, when the eruptive column reached 10 km high, producing a SO_2 total mass value equal to 22 kton.

Four different eruptive events, for which we have an almost simultaneous passage of TROPOMI, are highlighted in Figure 4. For these scenes, we report the comparison of our results with the Level 2 data, where the pixels contaminated by SO_2 are isolated, considering a detection flag > 0 (see Figure 5).

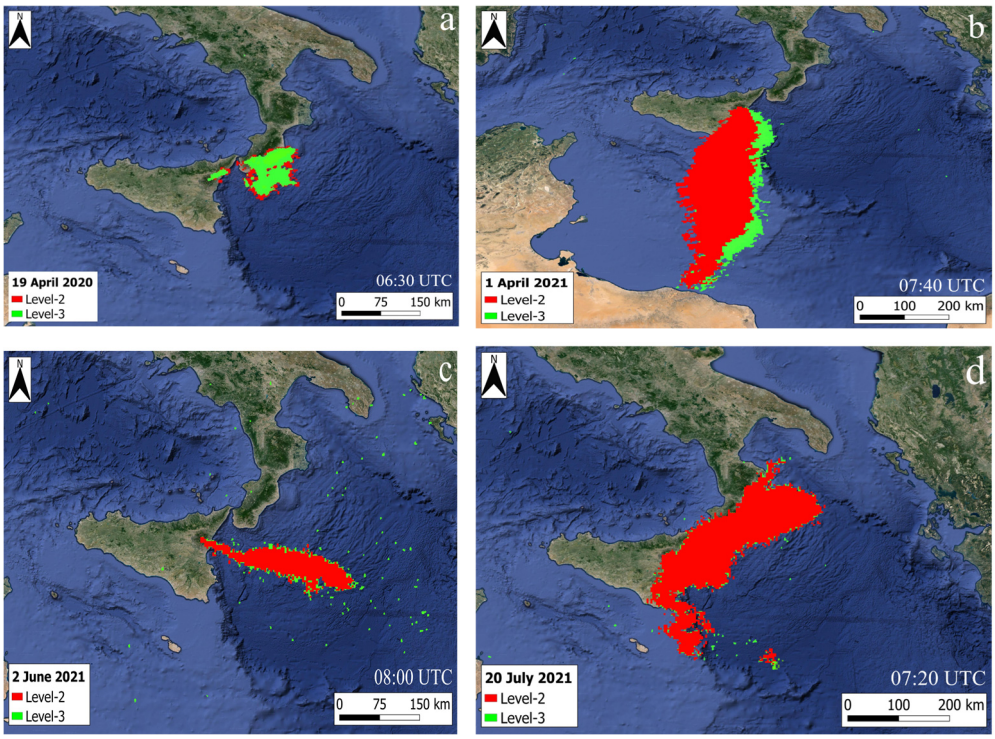

Figure 5. Volcanic SO_2 plume calculated around Mt. Etna during the paroxysmal events of (**a**) 19 April 2020 (started at 06:30 UTC), (**b**) 1 April 2021 (started at 07:40 UTC), (**c**) 2 June 2021 (started at 8:00 UTC) and (**d**) 20 July 2021 (started at 07:20 UTC). Shown in red is the plume derived from the Level 2 product, where a detection flag > 0 is applied, and in green is reported the result we obtained on GEE, exploiting the Level 3 product.

The episode on 19 April 2020 (Figure 5a) started at around 06:30 UTC, with Strombolian activity at the New South-East Crater, which gradually evolved into a modest lava fountain starting at 07:15 UTC. The activity occurred at one or two vents in the "Cono della Sella" area, formed in the spring of 2017, and initially produced mild ash emissions that progressively intensified from around 08:45 UTC. The eruptive activity generated a plume that rose up to approximately 5 km above sea level, with the prevailing winds driving it eastward. Ash fell on the volcano's eastern slope, primarily in the Valle del Bove, although lighter ash deposits were also reported in areas between Zafferana Etnea (on the southeastern slope) and Linguaglossa (on the northeastern slope). From 09:55 UTC onwards, the lava fountain activity gradually diminished until it ceased, and the significant ash emission progressively subsided. In correspondence with this eruption, we calculated a SO_2 total mass value of 0.40 kton, higher than the proximal values, which are all around 0, finding for example a mass of 0.068 kton on the date before the eruption. The detection limit for SO_2, in terms of the lowest concentration that can be reliably detected, is equal to 0.0000124 kton (https://sentiwiki.copernicus.eu, accessed on 1 September 2024). The calculated area on Level 2 is equal to 8565 km^2, whereas on L3 it is 6513 km^2. We also calculated the Jaccard index, given by the ratio between the intersection and the union of the two areas, finding a value of 0.72.

The activity on 1 April 2021 (Figure 5b), which had already begun at the end of March, was characterized by the formation of a lava fountain, producing an ash cloud that, at 07:40 UTC, had exceeded a height of approximately 9000 m above sea level, dispersing in the SSW direction. Here, we observed a value of 6.11 kton, whereas on the previous date we found a value of 0.11 kton and on the following date 1.24 kton. We estimated an area of 55,153 km^2 for L2 and equal to 58,948 km^2 for Level 3. The index of fitness is 0.68.

On 2 June 2021 (Figure 5c), an eruption began in the early hours of the day with Strombolian activity and developed into a robust lava fountain at the Southeast Crater (SEC), producing ash plume extending up to approximately 5–10 km above sea level and which dispersed in the east side. On this date, a value of 1.77 kton was calculated and the areas are, respectively, 10,200 km^2 for Level 2 and 11,352 km^2 for L3. The Jaccard index for this eruptive event is equal to 0.79.

The last eruption studied, where we found a value of 14.43 kton, refers to the activity occurring on 20 July 2021 (Figure 5d) that affected the SEC and during which was produced a lava fountain starting at 07:20 UTC. The products emitted were dispersed in the area between the southern and eastern sides of the volcano. Level 2 covers an area of 40,532 km^2, whereas Level 3 has a surface of 42,877 km^2. An index equal to 0.86 was calculated on this date.

For the eruptive events analyzed here in detail, we found an optimal correlation and fitting between the volcanic plume derived from the Level 2 products and the one calculated on GEE, as can also be seen from Figure 5. In general, our product (green colored) covers a larger area, mostly evident in the case study of 1 April 2021, where the fitness index is lower than the one calculated for the other cases analyzed. The only exception is represented by the event that occurred on 19 April 2020, where the plume from L2 covers a larger area.

Figure 6 shows the time series related to Sangay volcano, for which we reported the period from May 2020 to May 2021, characterized by many intense eruptive events.

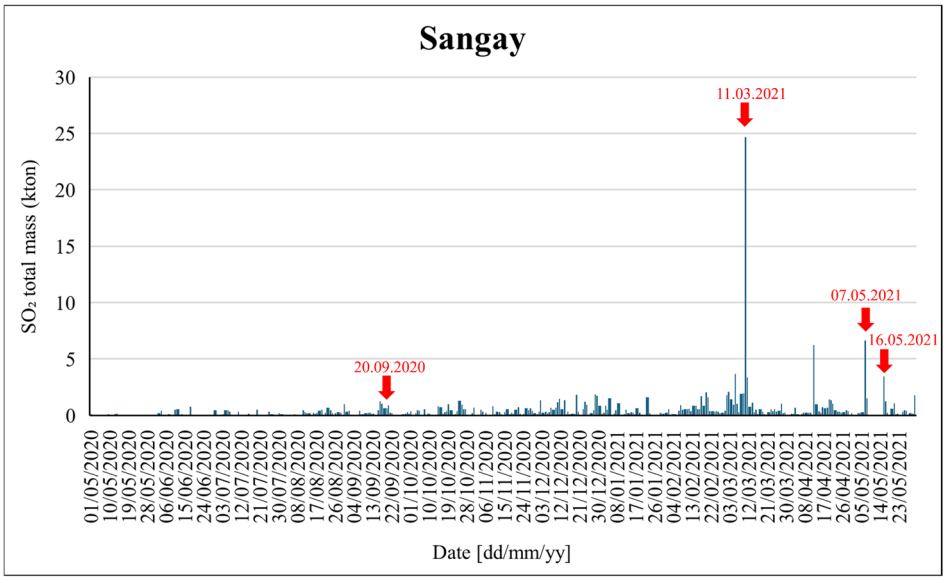

Figure 6. SO_2 total mass time series calculated for Sangay volcano, expressed in kton. The red arrows indicate the events analyzed in more detail.

Here, several peaks are also visible, and they are higher in 2021. We considered four eruptive events (among the most energetic in these two years and indicated by the red arrows in Figure 6), which are compared with the Level 2 product in Figure 7.

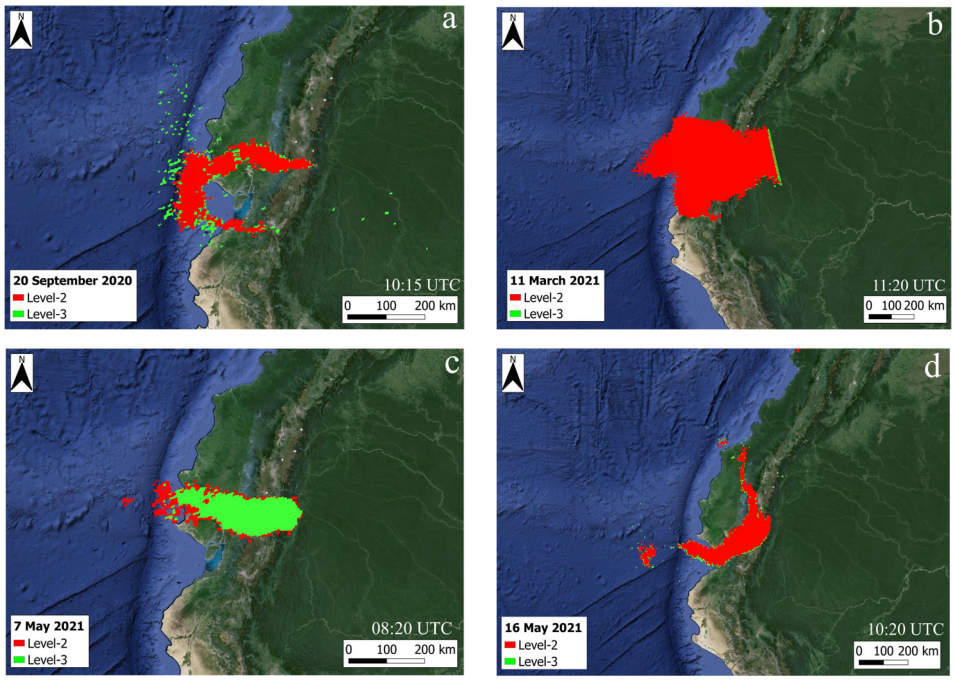

Figure 7. Volcanic SO_2 plume calculated for Sangay during the eruptive events of (**a**) 20 September 2020 (started at 10:15 UTC), (**b**) 11 March 2021 (started at 11:20 UTC), (**c**) 7 May 2021 (started at 08:20 UTC) and (**d**) 16 May 2021 (started at 10:20 UTC). In red, the plume derived from the Level 2 product, where a detection flag > 0 is applied; in green, the result we obtained on GEE, exploiting the Level 3 product.

Even in this case we found a good agreement between the volcanic plume derived from the Level 2 product and the one calculated with our method. As can be seen in Figure 7c, the case of 7 May 2021 shows a SO_2 plume derived from GEE that is smaller than the one derived from the Level 2 product.

The eruptive pulse on 20 September 2020, reported in Figure 7a, produced an eruptive column that quickly split into two parts: a higher, gas-rich cloud that rose to 15.2 km above sea level and moved east-southeast and a lower, ash-rich cloud at 12.2 km above sea level that drifted west. This resulted in ash fallout extending up to 280 km from the volcano (affecting the provinces of Chimborazo, Bolívar, Guayas and Los Ríos). On this date, a value of 0.63 kton of sulfur dioxide was calculated and we found areas of, respectively, 27,758 km^2 for Level 2 and 30,823 km^2 for Level 3. The Jaccard index for this eruptive event is equal to 0.72.

The date 11 March 2021 (see Figure 7b) was characterized by a large explosion that produced an ash plume reaching an altitude of 12.5 km. The eruption caused ash to spread extensively, up to 100 km west of the summit. The ashfall impacted several areas, including the Cantons of Guamote, Chambo, Riobamba, Penipe and Guano, with lighter ashfall reported in Colta, Alausí and Macas. The eruption generated a large sulfur dioxide (SO_2) plume, which was detected by satellite instruments, highlighting the explosive nature of the event (https://volcano.si.edu, accessed on 1 September 2024). The ash and debris flow from the eruption also caused significant disruptions, including an overflow of the Upano River dam due to mud and debris flows on 12 March. Volcanic activity continued, with steam and gas emissions observed a few days later on 14 March. Corresponding with this eruption, we calculated a SO_2 total mass value of 24.6 kton, which also represents the highest value of the entire series. Level 2 covers an area of 160,601 km^2, whereas Level 3 has a surface of 178,034 km^2. On this date, an index equal to 0.84 was calculated.

On 7 May 2021 (Figure 7c), the volcano underwent another significant eruption, during which an ash plume was reported to have reached up to 10.6 km in altitude. The ash cloud extended approximately 100 km west-southwest from the summit, affecting various regions. Significant ashfall was reported in several provinces, including Chimborazo, where it impacted communities such as Cebadas, Palmira, Punín and Colta (https://volcano.si.edu, accessed on 1 September 2024). Here, we calculated on GEE a value of 6 kton. We estimated an area of 34,679 km^2 for L2 and one equal to 25,603 km^2 regarding our result. The index of fitness is 0.71.

During the eruption of 16 May 2021 (Figure 7d), Sangay generated an ash plume that reached an estimated height of 11.3 km above sea level and drifted 140 km to the north. A lower-level plume also extended west-southwest, traveling 80 km from the summit at an altitude of 6.4 km. The ash cloud had considerable impacts, with ashfall reported in several provinces, including Chimborazo, Bolívar and Guayas, affecting agriculture in those areas (https://volcano.si.edu, accessed on 1 September 2024). In correspondence with this eruption, we calculated a SO_2 total mass value of 3.45 kton. The calculated area on the Level 2 product is equal to 42,888 km^2, whereas on L3 it is 43,565 km^2. The ratio between the intersection and the union of the two areas is equal to 0.77 on this date.

Figure 8 shows the time series related to Taal volcano, for which we reported the period from June 2021 to April 2022, characterized by several energetic eruptive events.

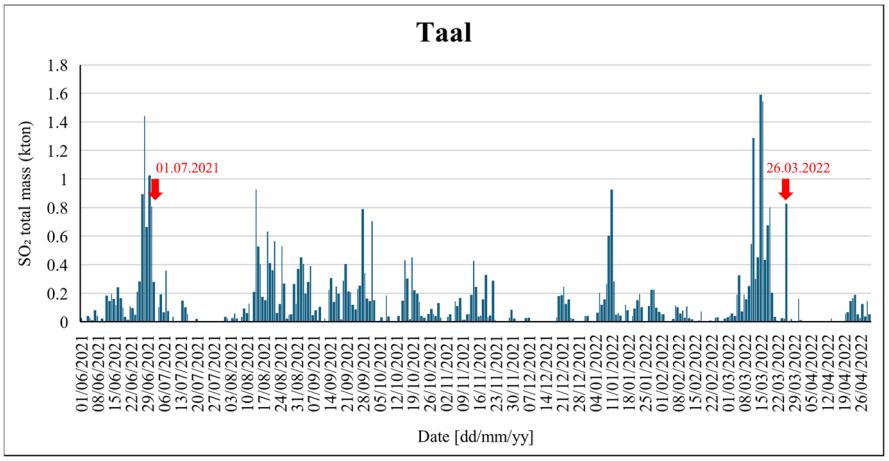

Figure 8. SO_2 total mass time series calculated on Taal volcano, expressed in kton. The red arrows indicate two of the four eruptive events analyzed in more detail, which are included in the selected time window.

Here, the highest SO_2 total mass value is calculated on 15 March 2022, as can be seen in Figure 8. On this date, a phreatomagmatic eruption produced an ash plume that rose 2400 m into the air, drifting southwest. This event was part of a series of similar eruptions and ongoing volcanic activity observed at Taal during this period (https://volcano.si.edu, accessed on 1 September 2024). We calculated a total sulfur dioxide mass of 1.6 kton in correspondence with this eruptive event.

The four episodes studied in detail are reported in Figure 9, where the comparison with the Level 2 product is performed.

First, we analyzed the 12–13 January 2020 eruption (Figure 9a) (not included in the time window in Figure), which was one of the most violent eruptions registered. It began on January 12 at 2:30 p.m. (local time) with an explosive event that produced a massive plume of volcanic ash reaching up to 15 km into the atmosphere. The ash spread as far as 67 km south of Manila and extended to Quezon City, about 70 km away from Taal. The eruption affected over 50,000 people, leading to the suspension of all flights at Manila

International Airport and the evacuation of Taal Island and the surrounding provinces. Within the first 24 h, the eruption triggered approximately 450 earthquakes, causing fissures to open and the surrounding lake to recede [113]. In correspondence with this eruption, we found a SO_2 total mass value of 170 kton, calculated on 13 January 2020. Level 2 covers an area of about 1,120,722 km^2, while the area resulting from GEE is equal to 1,460,524 km^2. The index of fitness calculated is 0.72.

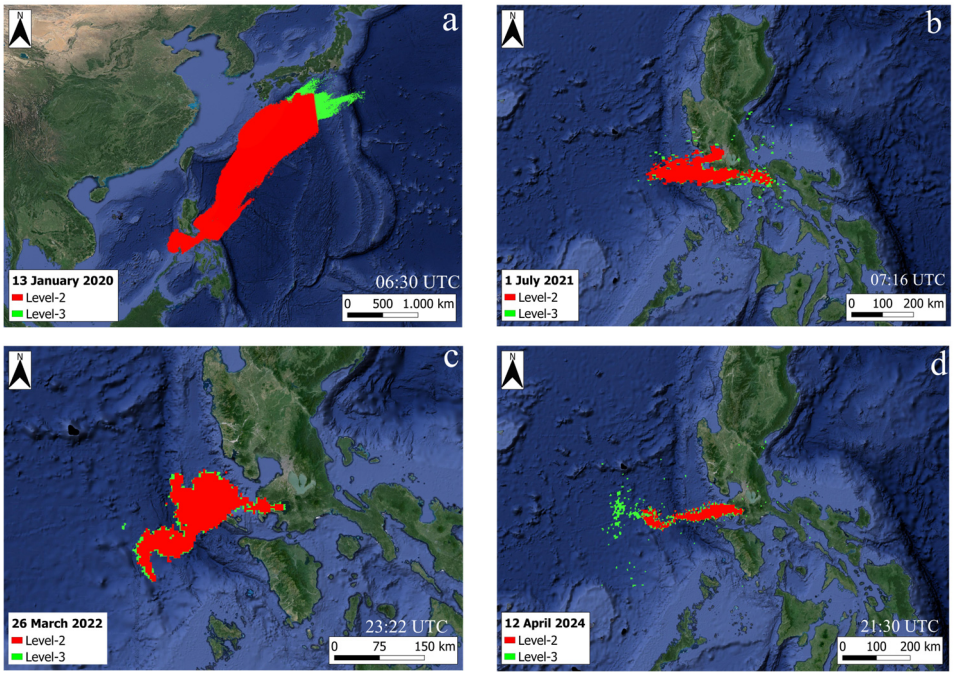

Figure 9. Volcanic SO_2 plume calculated on Taal volcano during the eruptions of (**a**) 12–13 January 2020 (started on 12 January at 06:30 UTC), (**b**) 1 July 2021 (started at 07:16 UTC), (**c**) 25–26 March 2022 (started on 25 March at 23:22 UTC) and (**d**) 11–12 April 2024 (started on 11 April at 21:30 UTC). In red, the plume derived from the Level 2 product, where a detection flag > 0 is applied: in green, the result we obtained on GEE, exploiting the Level 3 product.

We then focused on the eruption of 1st July 2021 (Figure 9b), which at 03:16 p.m. (local time) produced a dark gray phreatomagmatic plume that rose 1 km above the lake and lasted for about 5 min, prompting PHIVOLCS to raise the Volcano Alert Level from 2 to 3 (on a scale 0–5) at 03:37 p.m. (local time). The explosion followed strong SO_2 emissions on 28 June and 1 July, with rates of 14,241 and 13,287 t/d, respectively. Subsequent phreatomagmatic events, each lasting no more than two minutes, generated jetted plumes reaching 200 m above the Main Crater Lake. Between 1 and 2 July, the seismic network detected twenty-nine volcanic earthquakes, including one explosion, twenty-two low-frequency earthquakes and two volcanic tremors (https://volcano.si.edu, accessed on 1 September 2024). Corresponding with this eruption, we found a SO_2 total mass value of 0.8 kton. The calculated area on the Level 2 product is equal to 20,438 km^2, whereas on Level 3 it is 20,931 km^2. The index given by the ratio between the intersection and the union of the two areas is equal to 0.72.

The third eruption we considered was the one occurring on 25–26 March 2022 (Figure 9c), which consisted of a phreatomagmatic eruption that produced 66 explosions and prompted PHIVOLCS to raise the Alert Level to 3. Eruption plumes rose as high as 3 km. The National Disaster Risk Reduction and Management Council (NDRRMC) reported that by 27 March 2961 people had been evacuated. Here, we calculated a SO_2 total mass value equal to 0.82 kton, much higher than the near values, which were all around

0. We measured an area of 13,600 km^2 on Level 2 and a surface of 14,212 km^2 on Level 3. Corresponding with this eruption, an index equal to 0.85 was calculated.

Finally, we analyzed the eruption of 11–12 April 2024 (Figure 9d). On this date, Taal volcano underwent a series of five phreatic eruptions. The first eruption occurred between 5:11 and 5:24 a.m., producing a steam-laden plume that rose approximately 2400 m into the air and drifted southwest. Subsequent eruptions throughout the day, from 9:45 a.m. to 3:22 p.m., generated plumes rising between 100 and 300 m. These eruptions originated from a new vent on the southwest side of the main crater. A sixth phreatic eruption was recorded on April 13, producing a steam plume that rose 600 m and drifted west-northwest (https://volcano.si.edu, accessed on 1 September 2024). On this date, we found a value of 0.36 kton. The calculated surface on the Level 2 product here is equal to 7644 km^2, whereas on Level 3 it is 11,642 km^2. The index given by the ratio between the intersection and the union of the two areas is equal to 0.53.

Also, in this case study there is an optimal correlation between the volcanic plume derived from the Level 2 products and the one calculated on GEE. The plume resulting from Level 3 is bigger in the four events; this is mostly evident on 12 April 2024 and on 13 January 2020, where, however, the Level 2 product results are truncated on the Copernicus browser (https://browser.dataspace.copernicus.eu, accessed on 1 September 2024).

4. Discussion

The continuous release of sulfur dioxide with volcanic origins into the atmosphere is a source of danger, and its monitoring can be very useful for risk mitigation purposes. The arrival of the TROPOMI sensor onboard the Sentinel-5P satellite has allowed the identification of sulfur dioxide gas plumes with unprecedented resolution.

In this work, we implemented a new tool, exploiting the GEE Platform to have a rapid response in terms of SO_2 total mass from 2018 (the first year in which the images were available) to date, extrapolating a complete time series and characterizing eruption days that show higher values. GEE allows us to perform computations on a massive scale, making it easier to run large spatial analyses. The availability of the complete TROPOMI collection significantly reduces elaboration times, since users do not need to download the dataset or to install any software to perform the processing tasks. The need for a new tool emerges from the fact that applying a fixed threshold to the L3 TROPOMI product does not accurately represent the plume. The fixed threshold approach can indeed result in excessive scattering in some instances, while in others, it only captures pixels with high concentrations of SO_2, thereby introducing errors of up to 100% in total mass estimations. In contrast, the proposed method enhances plume continuity by firstly segmenting and then clustering pixels with similar characteristics, thereby providing a more accurate representation. Our method further reduces computational times due to the application of GEE-embedded techniques, thus providing annual time series in a few minutes.

We also introduced a density threshold equal to 0.00028 mol/m^2, defined as the ratio between the total mass value of SO_2 (given by the sum of the SO_2 values of each pixel for each class) and the relative number of pixels contained in each class, which was optimal for highlighting SO_2-contaminated pixels on all analyzed dates and for all case studies.

We apply our technique to Mount Etna (Italy), Sangay (Ecuador) and Taal (Philippines), which are three highly active open-conduit volcanoes. In particular, we exploit the TROPOMI Level 3 image collection available on GEE to compute the SO_2 total mass associated with active volcanic fields on a global scale. With respect to the commonly used Level 2 product, the Level 3 product does not have any mask for SO_2 identification; moreover, it is oversampled at 1 km and is available only at 0 and 15 km asl.

To evaluate the quality of our results based on the Level 3 product, we performed a comparison with the SO_2 mass data available from Level 2. In particular, we exploit the open-access web app "SO_2 Flux Calculator" developed by Grandin et al. [72] (https://dataviz.icare.univ-lille.fr/so2-flux-calculator, accessed on 1 September 2024). To have an effective comparison, the mass calculated at a 15 km height is considered within a radius of 300 km around Mt. Etna and Sangay and 200 km around the Taal volcano, similar to the areas defined on GEE for these three case studies. We selected those data with a solar zenith angle < 60° and quality > 0.5, as for the Level 3 data on GEE (see Section 2). Figure 10 reports the histograms relating to the differences obtained comparing our results and those provided by the platform for each volcano under study.

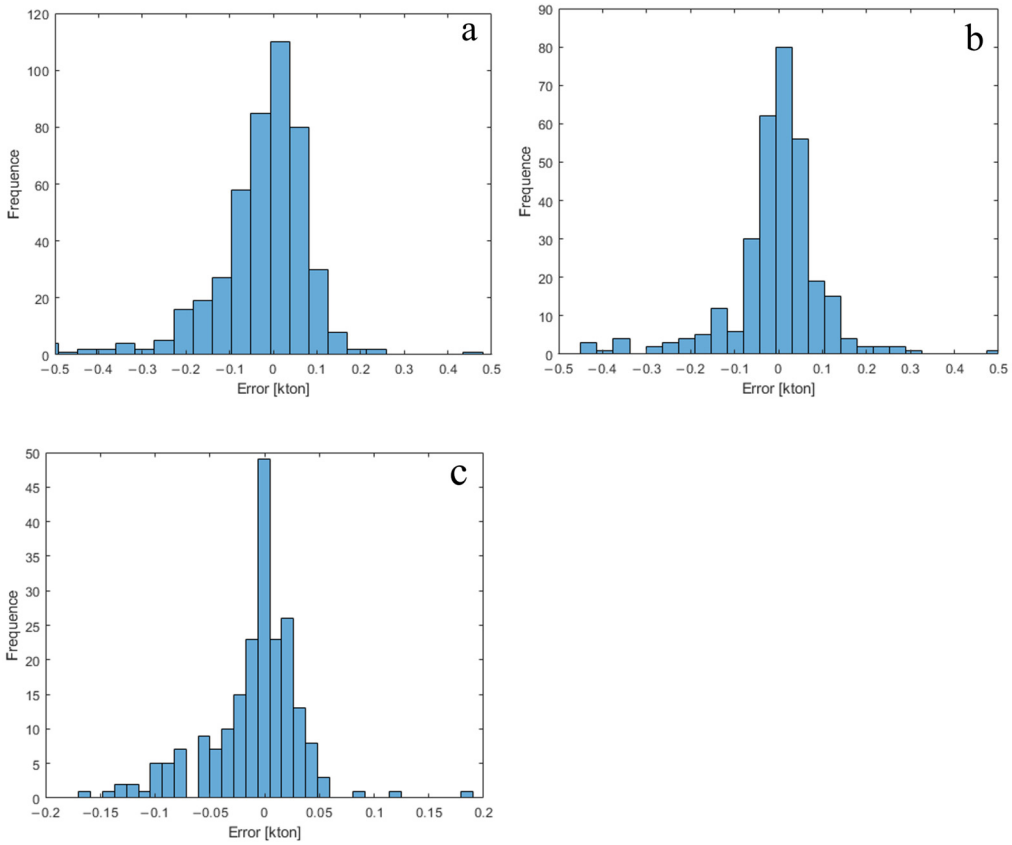

Figure 10. Histograms representing the difference between SO_2 total mass (expressed in kton) calculated on GEE and data from the "SO_2 Flux Calculator" application for Mt. Etna (**a**), Sangay (**b**) and Taal volcano (**c**).

In general, there is a good agreement between our results and the Level 2 results for the three volcanoes under investigation.

As for Mt. Etna (Figure 10a), we found that 90% of the data are between −0.06 and +0.06 kton and 75% of the values are included in the interval from −0.02 to +0.02 kton. The median is equal to −0.04 kton, the mean value corresponds to −0.25 kton and the standard deviation was calculated as 1.02 kton.

The Sangay volcano (Figure 10b) shows that 90% of the values lie between −0.08 and +0.08 kton, while the 75th percentile was calculated to be 0.04 kton. In this case, a median of 0.0007 kton was calculated, the mean value is −0.05 kton and the standard deviation is 0.6 kton.

The Taal volcano (Figure 10c) represents the case study in which the lowest error was found, with 90% of the data being between −0.02 and +0.02 kton and 75% of the values

being in the window between −0.01 and +0.01 kton. The calculated median is −0.0034 kton, the mean value is −0.02 kton and the standard deviation is 0.09 kton.

For all the cases, the median value of the difference is always below 0.04 kton; however, the plume calculated on GEE is often slightly larger than that calculated with Level 2 data, as can also be seen in the three left-skewed histograms.

In our case studies, the GEE product proved to be a solid choice for studying eruptive plumes, since the three volcanoes under study generally produce high eruptive columns (usually greater than 8 km a.s.l.) and can therefore be appreciated by exploiting the Level 3 product at 15 km. However, lower volcanic plumes could be inaccurately estimated on GEE. This is because the Level 3 product available lacks the layer at 7 km usually provided with Level 2 data. This problem should be overcome in the near future, when the 1 km and 7 km altitude products, usually used for interpolation with the product at 15 km, will be available.

Our method allows an easy and fast extrapolation of SO_2 data on an open-access platform. Moreover, the wide availability of libraries on GEE, together with the values of parameters provided in this work, make this method easy to apply, enabling users to reduce the time processing of the images.

Compared to other approaches in which GEE has been used (e.g., [114,115]), this method exploits AI techniques to more accurately identify the SO_2 cloud and derive the total SO_2 mass. It also provides longer time series, which allows visualization of any variations over time.

The tool we have implemented is a valid and accurate way to obtain data on the total mass of SO_2, reducing delays and improving calculation times. Furthermore, since GEE contains the entire TROPOMI collection on a global scale, our method can be easily applied to volcanoes all over the world, simply by varying the input geometry.

Author Contributions: Conceptualization, G.G.; methodology, G.G. and M.D.; software, M.D.; validation, A.A. and A.C.; formal analysis, M.D. and G.B.; investigation, M.D., G.B. and A.A.; resources, A.A. and G.G.; data curation, M.D.; writing—original draft preparation, M.D. and G.G.; writing—review and editing, M.D., A.C., G.G., G.B. and A.A.; visualization, M.D.; supervision, A.A. and G.G. All authors have read and agreed to the published version of the manuscript.

Funding: This work was supported by the INGV project Pianeta Dinamico (grant number: CUP D53J19000170001) funded by the Italian Ministry of University and Research ("Fondo finalizzato al rilancio degli investimenti delle amministrazioni centrali dello Stato e allo sviluppo del Paese", legge 145/2018), Volcanological Theme SAFARI (An Artificial Intelligence-based StrAtegy For volcAno hazaRd monItoring from space).

Data Availability Statement: The Sentinel-5P Level 2 imagery used in this work was provided by the Copernicus Browser. The programming code developed on GEE and the datasets generated during this study are available from the corresponding author upon request.

Acknowledgments: The authors gratefully thank the Copernicus Browser (https://scihub.copernicus.eu/; accessed on 1 September 2024) for providing the Sentinel-5P Level 2 imagery to this study and the Istituto Nazionale di Geofisica e Vulcanologia, Italy, grant "Progetto INGV Pianeta Dinamico VT SAFARI 2023-24" funded by Italian Ministry MIUR ("Fondo Finalizzato al rilancio degli investimenti delle amministrazioni centrali dello Stato e allo sviluppo del Paese", legge 145/2018). The English style was corrected by Stephen Conway.

Conflicts of Interest: The authors declare no conflicts of interest.

References

1. Carn, S.A.; Fioletov, V.E.; McLinden, C.A.; Li, C.; Krotkov, N.A. A Decade of Global Volcanic SO_2 Emissions Measured from Space. *Sci. Rep.* **2017**, *7*, 44095. [CrossRef] [PubMed]
2. Oppenheimer, C.; Scaillet, B.; Martin, R.S. Sulfur Degassing From Volcanoes: Source Conditions, Surveillance, Plume Chemistry and Earth System Impacts. *Rev. Mineral. Geochem.* **2011**, *73*, 363–421. [CrossRef]
3. Chin, M.; Jacob, D.J. Anthropogenic and Natural Contributions to Tropospheric Sulfate: A Global Model Analysis. *J. Geophys. Res. Atmos.* **1996**, *101*, D17. [CrossRef]
4. Oppenheimer, C.; Kyle, P.; Eisele, F.; Crawford, J.; Huey, G.; Tanner, D.; Kim, S.; Maudlin, L.; Blake, D.; Beyersdorf, A.; et al. Atmospheric Chemistry of an Antarctic Volcanic Plume. *J. Geophys. Res. Atmos.* **2010**, *115*, D04303. [CrossRef]
5. Thordarson, T.; Self, S. Atmosphere and Environmental Effects of the 1783-1784 Laki Eruption: A Review and Reassessment. *J. Geophys. Res. Atmos.* **2003**, *108*, D1. [CrossRef]
6. Wilson, R.J.S.; Miles, D.; Loader, N.; Melvin, T.M.; Cunningham, L.; Cooper, R.J.; Briffa, K. A Millennial Long March–July Precipitation Reconstruction for Southern-Central England. *Clim. Dyn.* **2012**, *38*, 5. [CrossRef]
7. Hutchinson, T.C.; Whitby, L.M. The Effects of Acid Rainfall and Heavy Metal Particulates on a Boreal Forest Ecosystem near the Sudbury Smelting Region of Canada. *Water Air Soil Pollut.* **1977**, *7*, 421–438. [CrossRef]
8. Dentener, F.; Drevet, J.; Lamarque, J.F.; Bey, I.; Eickhout, B.; Fiore, A.M.; Hauglustaine, D.; Horowitz, L.W.; Krol, M.; Kulshrestha, U.C.; et al. Nitrogen and Sulfur Deposition on Regional and Global Scales: A Multimodel Evaluation. *Glob. Biogeochem. Cycles* **2006**, *20*, 4. [CrossRef]
9. Vet, R.; Artz, R.S.; Carou, S.; Shaw, M.; Ro, C.U.; Aas, W.; Baker, A.; Bowersox, V.C.; Dentener, F.; Galy-Lacaux, C.; et al. A Global Assessment of Precipitation Chemistry and Deposition of Sulfur, Nitrogen, Sea Salt, Base Cations, Organic Acids, Acidity and pH, and Phosphorus. *Atmos. Environ.* **2014**, *93*, 3–100. [CrossRef]
10. Fedkin, N.; Li, C.; Dickerson, R.R.; Canty, T.; Krotkov, N.A. Linking Improvements in Sulfur Dioxide Emissions to Decreasing Sulfate Wet Deposition by Combining Satellite and Surface Observations with Trajectory Analysis. *Atmos. Environ.* **2018**, *199*, 210–223. [CrossRef]
11. Casadevall, T.J. Volcanic Ash and Aviation Safety; Proceedings of the First International Symposium on Volcanic Ash and Aviation Safety. *U.S. Geol. Surv. Bull.* **1994**, *2047*, 1–450. [CrossRef]
12. Baxter, P.J.; Ing, R.; Falk, H.; French, J.; Stein, G.F.; Bernstein, R.S.; Merchant, J.A. Mount St. Helens Eruptions, May 18 to June 12, 1980. An Overview of the Acute Health Impact. *JAMA* **1982**, *246*, 2585–2589. [CrossRef]
13. Horwell, C.J.; Baxter, P.J. The Respiratory Health Hazards of Volcanic Ash: A Review for Volcanic Risk Mitigation. *Bull. Volcanol.* **2006**, *69*, 1–24. [CrossRef]
14. Klimont, Z.; Smith, S.J.; Cofala, J. The Last Decade of Global Anthropogenic Sulfur Dioxide: 2000–2011 Emissions. *Environ. Res. Lett.* **2013**, *8*, 014003. [CrossRef]
15. Smith, S.J.; van Aardenne, J.; Klimont, Z.; Andres, R.J.; Volke, A.; Delgado Arias, S. Anthropogenic Sulfur Dioxide Emissions: 1850–2005. *Atmos. Chem. Phys.* **2011**, *11*, 1101–1116. [CrossRef]
16. Scaillet, B.; Clemente, B.; Evans, B.W.; Pichavant, M. Redox Control of Sulfur Degassing in Silicic Magmas. *J. Geophys. Res. Atmos.* **1998**, *103*, 23937–23950. [CrossRef]
17. Shinohara, H. Excess Degassing from Volcanoes and Its Role on Eruptive and Intrusive Activity. *Rev. Geophys.* **2008**, *46*, RG4005. [CrossRef]
18. Fischer, T.P.; Arellano, S.; Carn, S.; Aiuppa, A.; Galle, B.; Allard, P.; Lopez, T.; Shinohara, H.; Kelly, P.; Werner, C.; et al. The Emissions of CO_2 and Other Volatiles from the World's Subaerial Volcanoes. *Sci. Rep.* **2019**, *9*, 18716. [CrossRef]
19. Hansell, A.; Oppenheimer, C. Health Hazards from Volcanic Gases: A Systematic Literature Review. *J. Expo. Sci. Environ. Epidemiol.* **2010**, *15*, 628–639. [CrossRef] [PubMed]
20. Longo, B.M.; Grunder, A.; Chuan, R.; Rossignol, A. SO_2 and Fine Aerosol Dispersion from the Kilauea Plume, Kau District, Hawaii, USA. *Geology* **2005**, *33*, 217–220. [CrossRef]
21. Robock, A. Volcanic eruptions and climate. *Rev. Geophys.* **2000**, *38*, 191–219. [CrossRef]
22. Marshall, L.R.; Maters, E.C.; Schmidt, A.; Timmreck, C.; Robock, A.; Toohey, M. Volcanic effects on climate: Recent advances and future avenues. *Bull. Volcanol.* **2022**, *84*, 54. [CrossRef]
23. Delgado-Granados, H.; Cárdenas González, L.; Sánchez, N.P. Sulfur dioxide emissions from Popocatépetl volcano (Mexico): Case study of a high-emission rate, passively degassing erupting volcano. *J. Volcanol. Geotherm. Res.* **2001**, *108*, 107–120. [CrossRef]
24. Ganci, G.; Cappello, A.; Bilotta, G.; Del Negro, C. How the variety of satellite remote sensing data over volcanoes can assist hazard monitoring efforts: The 2011 eruption of Nabro volcano. *Remote Sens. Environ.* **2020**, *236*, 111426. [CrossRef]
25. Calvari, S.; Ganci, G.; Victória, S.S.; Hernandez, P.A.; Perez, N.M.; Barrancos, J.; Alfama, V.; Dionis, S.; Cabral, J.; Cardoso, N.; et al. Satellite and ground remote sensing techniques to trace the hidden growth of a lava flow field: The 2014–2015 effusive eruption at Fogo volcano (Cape Verde). *Remote Sens.* **2018**, *10*, 1115. [CrossRef]
26. Allard, P. Endogenous magma degassing and storage at Mount Etna. *Geophys. Res. Lett.* **1997**, *24*, 2219–2222. [CrossRef]

27. Sutton, A.J.; Elias, T.; Gerlach, T.M.; Stokes, J.B. Implications for eruptive processes as indicated by sulfur dioxide emission from Kīlauea Volcano, Hawai'i, 1979–1997. *J. Volcanol. Geotherm. Res.* **2001**, *108*, 283–302. [CrossRef]
28. Edmonds, M.; Herd, R.A.; Galle, B.; Oppenheimer, C.M. Automated, high time-resolution measurements of SO_2 flux at Soufrière Hills Volcano, Montserrat. *Bull. Volcanol.* **2003**, *65*, 578–586. [CrossRef]
29. Palma, J.L.; Calder, E.S.; Basualto, D.; Blake, S.; Rothery, D.A. Correlations between SO_2 flux, seismicity, and outgassing activity at the open vent of Villarrica volcano, Chile. *J. Geophys. Res.* **2008**, *113*, B10. [CrossRef]
30. Caltabiano, T.; Burton, M.; Giammanco, S.; Allard, P.; Bruno, N.; Murè, F.; Romano, R. Volcanic gas emissions from the summit craters and flanks of Mt. Etna, 1987–2000. *Mt. Etna Volcano Lab.* **2004**, *143*, 111–128. [CrossRef]
31. Burton, M.R.; Caltabiano, T.; Murè, F.; Salerno, G.; Randazzo, D. SO_2 flux from Stromboli during the 2007 eruption: Results from the FLAME network and traverse measurements. *J. Volcanol. Geotherm. Res.* **2009**, *182*, 214–220. [CrossRef]
32. Aiuppa, A.; Lo Bue Trisciuzzi, G.; Alparone, S.; Bitetto, M.; Coltelli, M.; Delle Donne, D.; Ganci, G.; Pecora, E. A SO_2 flux study of the Etna volcano 2020–2021 paroxysmal sequences. *Front. Earth Sci.* **2023**, *11*, 1115111. [CrossRef]
33. Arellano, S.; Galle, B.; Apaza, F.; Avard, G.; Barrington, C.; Bobrowski, N.; Bucarey, C.; Burbano, V.; Burton, M.; Chacón, Z.; et al. Synoptic analysis of a decade of daily measurements of SO_2 emission in the troposphere from volcanoes of the global ground-based Network for Observation of Volcanic and Atmospheric Change. *Earth Syst. Sci. Data* **2021**, *13*, 1167–1188. [CrossRef]
34. Loughlin, S.C.; Vye-Brown, C.; Sparks, R.S.J.; Brown, S.K.; Barclay, J.; Calder, E.; Cottrell, E.; Jolly, G.; Komorowski, J.-C.; Mandeville, C.; et al. An introduction to global volcanic hazard and risk. In *Global Volcanic Hazards and Risk*; Cambridge University Press: Cambridge, UK, 2015; pp. 1–80. [CrossRef]
35. Boichu, M.; Clarisse, L.; Péré, J.-C.; Herbin, H.; Goloub, P.; Thieuleux, F.; Ducos, F.; Clerbaux, C.; Tanré, D. Temporal variations of flux and altitude of sulfur dioxide emissions during volcanic eruptions: Implications for long-range dispersal of volcanic clouds. *Atmos. Chem. Phys.* **2015**, *15*, 8381–8400. [CrossRef]
36. Kern, D.; Moser, R.; Hartmann, E.; Moder, M. Supply risk management: Model development and empirical analysis. *Int. J. Phys. Distrib. Logist. Manag.* **2012**, *42*, 60–82. [CrossRef]
37. Platt, U.; Stutz, J. *Differential Optical Absorption Spectroscopy (DOAS)—Principles and Applications*; Springer: Berlin/Heidelberg, Germany, 2008. [CrossRef]
38. Krueger, A.J. Sighting of El Chichon sulfur dioxide with the Nimbus-7 total ozone mapping spectrometer. *Science* **1983**, *220*, 1377–1378. [CrossRef]
39. Eisinger, M.; Burrows, J.P. Tropospheric Sulfur Dioxide observed by the ERS-2 GOME instrument. *Geophys. Res. Lett.* **1998**, *25*, 4177–4180. [CrossRef]
40. Khokhar, M.F.; Frankenberg, C.; Van Roozendael, M.; Beirle, S.; Kühl, S.; Richter, A.; Platt, U.; Wagner, T. Satellite observations of atmospheric SO_2 from volcanic eruptions during the time-period of 1996–2002. *Adv. Space Res.* **2005**, *36*, 879–887. [CrossRef]
41. Bovensmann, H.; Burrows, J.P.; Buchwitz, M.; Frerick, J.; Noël, S.; Rozanov, V.V.; Chance, K.V.; Goede, A.P.H. SCIAMACHY: Mission objectives and measurement modes. *J. Atmos. Sci.* **1999**, *56*, 127–150. [CrossRef]
42. Afe, O.T.; Richter, A.; Sierk, B.; Wittrock, F.; Burrows, J.P. BrO emission from volcanoes: A survey using GOME and SCIAMACHY measurements. *Geophys. Res. Lett.* **2004**, *31*, 23. [CrossRef]
43. Lee, C.; Martin, R.V.; van Donkelaar, A.; O'Byrne, G.; Krotkov, N.; Richter, A.; Huey, L.G.; Holloway, J.S. Retrieval of vertical columns of sulfur dioxide from SCIAMACHY and OMI: Air mass factor algorithm development, validation, and error analysis. *J. Geophys. Res. Atmos.* **2009**, *114*, D21. [CrossRef]
44. Krotkov, N.A.; Carn, S.A.; Krueger, A.J.; Bhartia, P.K.; Yang, K. Band residual difference algorithm for retrieval of SO_2 from the Aura Ozone Monitoring Instrument (OMI). *IEEE Trans. Geosci. Remote Sens.* **2006**, *44*, 1259–1266. [CrossRef]
45. Yang, K.; Krotkov, N.A.; Krueger, A.J.; Carn, S.A.; Bhartia, P.K.; Levelt, P.F. Retrieval of large volcanic SO_2 columns from the Aura Ozone Monitoring Instrument: Comparison and limitations. *J. Geophys. Res.* **2007**, *112*, D24S43. [CrossRef]
46. Li, C.; Krotkov, N.A.; Leonard, P.J.T.; Carn, S.; Joiner, J.; Spurr, R.J.D.; Vasilkov, A. Version 2 Ozone Monitoring Instrument SO_2 product ($OMSO_2$ V2): New anthropogenic SO_2 vertical column density dataset. *Atmos. Meas. Tech.* **2020**, *13*, 6175–6191. [CrossRef]
47. Theys, N.; de Smedt, I.; van Gent, J.; Danckaert, T.; Wang, T.; Hendrick, F.; Stavrakou, T.; Bauduin, S.; Clarisse, L.; Li, C.; et al. Sulfur dioxide vertical column DOAS retrievals from the Ozone Monitoring Instrument: Global observations and comparison to ground-based and satellite data. *J. Geophys. Res. Atmos.* **2015**, *120*, 2470–2491. [CrossRef]
48. Nowlan, C.R.; Liu, X.; Chance, K.; Cai, Z.; Kurosu, T.P.; Lee, C.; Martin, R.V. Retrievals of sulfur dioxide from the Global Ozone Monitoring Experiment 2 (GOME-2) using an optimal estimation approach: Algorithm and initial validation. *J. Geophys. Res. Atmos.* **2011**, *116*, D18. [CrossRef]
49. Rix, M.; Valks, P.; Hao, N.; Loyola, D.; Schlager, H.; Huntrieser, H.; Flemming, J.; Koehler, U.; Schumann, U.; Inness, A. Volcanic SO_2, BrO and plume height estimations using GOME-2 satellite measurements during the eruption of Eyjafjallajökull in 2010. *J. Geophys. Res. Atmos.* **2012**, *117*, D00U19. [CrossRef]
50. Hörmann, C.; Sihler, H.; Bobrowski, N.; Beirle, S.; Penning de Vries, M.; Platt, U.; Wagner, T. Systematic investigation of bromine monoxide in volcanic plumes from space by using the GOME-2 instrument. *Atmos. Chem. Phys.* **2013**, *13*, 4749–4781. [CrossRef]

51. Yang, K.; Dickerson, R.R.; Carn, S.A.; Ge, C.; Wang, J. First observations of SO_2 from the satellite Suomi NPP OMPS: Widespread air pollution events over China. *Geophys. Res. Lett.* **2013**, *40*, 18. [CrossRef]
52. Zhang, Y.; Li, C.; Krotkov, N.A.; Joiner, J.; Fioletov, V.; McLinden, C. Continuation of long-term global SO_2 pollution monitoring from OMI to OMPS. *Atmos. Meas. Tech.* **2017**, *10*, 1495–1509. [CrossRef]
53. Theys, N.; De Smedt, I.; Yu, H.; Danckaert, T.; van Gent, J.; Hörmann, C.; Wagner, T.; Hedelt, P.; Bauer, H.; Romahn, F.; et al. Sulfur dioxide retrievals from TROPOMI onboard Sentinel-5 Precursor: Algorithm theoretical basis. *Atmos. Meas. Tech.* **2017**, *10*, 119–153. [CrossRef]
54. Schoeberl, M.R.; Douglass, A.; Hilsenrath, E.; Bhartia, P.; Beer, R.; Waters, J.; Gunson, M.; Froidevaux, L.; Gille, J.; Barnett, J.; et al. Overview of the EOS Aura mission. *IEEE Trans. Geosci. Remote Sens.* **2006**, *44*, 1066–1074. [CrossRef]
55. Krotkov, N.A.; McLinden, C.A.; Li, C.; Lamsal, L.N.; Celarier, E.A.; Marchenko, S.V.; Swartz, W.H.; Bucsela, E.J.; Joiner, J.; Duncan, B.N.; et al. Aura OMI observations of regional SO_2 and NO_2 pollution changes from 2005 to 2015. *Atmos. Chem. Phys.* **2016**, *16*, 4605–4629. [CrossRef]
56. Veefkind, J.P.P.; Aben, I.; McMullan, K.; Förster, H.; de Vries, J.; Otter, G.; Claas, J.; Eskes, H.J.J.; de Haan, J.F.F.; Kleipool, Q.; et al. TROPOMI on the ESA Sentinel-5 Precursor: A GMES mission for global observations of the atmospheric composition for climate, air quality and ozone layer applications. *Remote Sens. Environ.* **2012**, *120*, 70–83. [CrossRef]
57. Fioletov, V.; McLinden, C.A.; Griffin, D.; Theys, N.; Loyola, D.G.; Hedelt, P.; Krotkov, N.A.; Li, C. Anthropogenic and volcanic point source SO_2 emissions derived from TROPOMI on board Sentinel-5 Precursor: First results. *Atmos. Chem. Phys.* **2020**, *20*, 5591–5607. [CrossRef]
58. Theys, N.; Hedelt, P.; De Smedt, I.; Lerot, C.; Yu, H.; Vlietinck, J.; Pedergnana, M.; Arellano, S.; Galle, B.; Fernandez, D.; et al. Global monitoring of volcanic SO_2 degassing with unprecedented resolution from TROPOMI onboard Sentinel-5 Precursor. *Sci. Rep.* **2019**, *9*, 2643. [CrossRef]
59. Pardini, F.; Burton, M.; de' Michieli Vitturi, M.; Corradini, S.; Salerno, G.; Merucci, L.; Di Grazia, G. Retrieval and intercomparison of volcanic SO_2 injection height and eruption time from satellite maps and ground-based observations. *J. Volcanol. Geotherm. Res.* **2017**, *331*, 79–91. [CrossRef]
60. Kleipool, Q.; Ludewig, A.; Babić, L.; Bartstra, R.; Braak, R.; Dierssen, W.; Dewitte, P.-J.; Kenter, P.; Landzaat, R.; Leloux, J.; et al. Pre-launch calibration results of the TROPOMI payload on-board the Sentinel-5 Precursor satellite. *Atmos. Meas. Tech.* **2018**, *11*, 6439–6479. [CrossRef]
61. Pardini, F.; Burton, M.; Arzilli, F.; La Spina, G.; Polacci, M. SO_2 emissions, plume heights and magmatic processes inferred from satellite data: The 2015 Calbuco eruptions. *J. Volcanol. Geotherm. Res.* **2018**, *361*, 12–24. [CrossRef]
62. Hedelt, P.; Efremenko, D.S.; Loyola, D.G.; Spurr, R.; Clarisse, L. Sulfur dioxide layer height retrieval from Sentinel-5 Precursor/TROPOMI using FP_ILM. *Atmos. Meas. Tech.* **2019**, *12*, 5503–5517. [CrossRef]
63. Queißer, M.; Burton, M.; Theys, N.; Pardini, F.; Salerno, G.; Caltiabiano, T.; Varnham, M.; Esse, B.; Kazahaya, R. TROPOMI enables high resolution SO_2 flux observations from Mt. Etna (Italy), and beyond. *Sci. Rep.* **2019**, *9*, 957. [CrossRef] [PubMed]
64. Ialongo, I.; Virta, H.; Eskes, H.; Hovila, J.; Douros, J. Comparison of TROPOMI/Sentinel-5 Precursor NO_2 observations with ground-based measurements in Helsinki. *Atmos. Meas. Tech.* **2020**, *13*, 205–218. [CrossRef]
65. Ludewig, A.; Kleipool, Q.; Bartstra, R.; Landzaat, R.; Leloux, J.; Loots, E.; Meijering, P.; van der Plas, E.; Rozemeijer, N.; Vonk, F.; et al. In-flight calibration results of the TROPOMI payload on board the Sentinel-5 Precursor satellite. *Atmos. Meas. Tech.* **2020**, *13*, 3561–3580. [CrossRef]
66. Burton, M.; Hayer, C.; Miller, C.; Christenson, B. Insights into the 9 December 2019 eruption of Whakaari/White Island from analysis of TROPOMI SO_2 imagery. *Sci. Adv.* **2021**, *7*, eabg1218. [CrossRef] [PubMed]
67. Cofano, A.; Cigna, F.; Santamaria Amato, L.; Siciliani de Cumis, M.; Tapete, D. Exploiting Sentinel-5P TROPOMI and Ground Sensor Data for the Detection of Volcanic SO_2 Plumes and Activity in 2018–2021 at Stromboli, Italy. *Sensors* **2021**, *21*, 6991. [CrossRef]
68. Pandey, P.C. Highlighting the role of earth observation Sentinel-5P TROPOMI in monitoring volcanic eruptions: A report on Hunga Tonga, a Submarine Volcano. *Remote Sens. Lett.* **2022**, *13*, 912–923. [CrossRef]
69. Wang, C.; Wang, T.; Wang, P.; Wang, W. Assessment of the Performance of TROPOMI NO_2 and SO_2 Data Products in the North China Plain: Comparison, Correction and Application. *Remote Sens.* **2022**, *14*, 214. [CrossRef]
70. De Santis, D.; Petracca, I.; Corradini, S.; Guerrieri, L.; Picchiani, M.; Merucci, L.; Stelitano, D.; Del Frate, F.; Prata, F.; Schiavon, G. Volcanic SO_2 Near-Real Time Retrieval Using Tropomi Data and Neural Networks: The December 2018 Etna Test Case. In Proceedings of the IEEE International Geoscience and Remote Sensing Symposium IGARSS, Brussels, Belgium, 11–16 July 2021; pp. 8480–8483. [CrossRef]
71. Markus, B.; Valade, S.; Wöllhaf, M.; Hellwich, O. Automatic retrieval of volcanic SO_2 emission source from TROPOMI products. *Front. Earth Sci.* **2023**, *10*, 1064171. [CrossRef]
72. Grandin, R.; Boichu, M.; Mathurin, T.; Pascal, N. Automatic Estimation of Daily Volcanic Sulfur Dioxide Gas Flux From TROPOMI Satellite Observations: Application to Etna and Piton de la Fournaise. *JRC Solid Earth* **2024**, *129*, 6. [CrossRef]

73. Shinoara, H. Volatile flux from subduction zone volcanoes: Insights from a detailed evaluation of the fluxes from volcanoes in Japan. *J. Volcanol. Geotherm. Res.* **2013**, *268*, 46–63. [CrossRef]
74. Delos Reyes, P.J.; Bornas, M.A.V.; Dominey-Howes, D.; Pidlaoan, A.C.; Magill, C.R.; Solidum, R.U., Jr. A synthesis and review of historical eruptions at Taal Volcano, Southern Luzon, Philippines. *Earth-Sci. Rev.* **2018**, *177*, 565–588. [CrossRef]
75. Bato, M.G.; Lundgren, P.; Pinel, V.; Solidum, R., Jr.; Daag, A.; Cahulogan, M. The 2020 Eruption and Large Lateral Dike Emplacement at Taal Volcano, Philippines: Insights From Satellite Radar Data. *Geophys. Res. Lett.* **2021**, *48*, 7. [CrossRef]
76. Valverde, V.; Mothes, P.A.; Beate, B.; Bernard, J. Enormous and far-reaching debris avalanche deposits from Sangay volcano (Ecuador): Multidisciplinary study and modeling the 30 ka sector collapse. *J. Volcanol. Geotherm. Res.* **2021**, *411*, 107172. [CrossRef]
77. Bernard, B.; Samaniego, P.; Mastin, L.; Hernandez, S.; Pino, G.; Kibler, J.; Encalada, M.; Hidalgo, S.; Vizuete, N. Forecasting and communicating the dispersion and fallout of ash during volcanic eruptions: Lessons from the September 20, 2020 eruptive pulse at Sangay volcano Ecuador. *Front. Earth Sci.* **2022**, *10*, 912835. [CrossRef]
78. Vasconez, F.J.; Hidalgo, S.; Battaglia, J.; Hernandez, S.; Bernard, B.; Coppola, D.; Valade, S.; Ramón, P.; Arellano, S.; Liorzou, C.; et al. Linking ground-based data and satellite monitoring to understand the last two decades of eruptive activity at Sangay volcano Ecuador. *Bull. Volcanol.* **2022**, *84*, 49. [CrossRef]
79. Theys, N.; Fioletov, V.; Li, C.; De Smedt, I.; Lerot, C.; McLinden, C.; Krotkov, N.; Griffin, D.; Clarisse, L.; Hedelt, P.; et al. A sulfur dioxide Covariance-Based Retrieval Algorithm (COBRA): Application to TROPOMI reveals new emission sources. *Atmos. Chem. Phys.* **2021**, *21*, 16727–16744. [CrossRef]
80. Khairunnisa, K.; Asti Anggari, E.; Rahayu, D.A.; Herawan, A.; Soedjarwo, M.; Tri Judianto, C. Superpixel-Based Stripe Noise Removal for Satellite Imageries. *J. Nas. Tek. Elektro Dan Teknol. Inf.* **2023**, *12*, 124–130. [CrossRef]
81. Yang, L.; Mansaray, L.R.; Huang, J.; Wang, L. Optimal Segmentation Scale Parameter, Feature Subset and Classification Algorithm for Geographic Object-Based Crop Recognition Using Multisource Satellite Imagery. *Remote Sens.* **2019**, *11*, 514. [CrossRef]
82. Csillik, O. Fast segmentation and classification of very high resolution remote sensing data using SLIC superpixels. *Remote Sens.* **2017**, *9*, 243. [CrossRef]
83. Gong, Y.; Zhou, Y. Differential evolutionary superpixel segmentation. *IEEE Trans. Image Process.* **2017**, *27*, 1390–1404. [CrossRef] [PubMed]
84. Duro, D.C.; Franklin, S.E.; Dubé, M.G. A comparison of pixel-based and object-based image analysis with selected machine learning algorithms for the classification of agricultural landscapes using SPOT-5 HRG imagery. *Remote Sens. Environ.* **2012**, *118*, 259–272. [CrossRef]
85. Ma, L.; Cheng, L.; Li, M.; Liu, Y.; Ma, X. Training set size, scale, and features in Geographic Object-Based Image Analysis of very high resolution unmanned aerial vehicle imagery. *ISPRS J. Photogramm.* **2015**, *102*, 14–27. [CrossRef]
86. Qu, L.; Chen, Z.; Li, M.; Zhi, J.; Wang, H. Accuracy Improvements to Pixel-Based and Object-Based LULC Classification with Auxiliary Datasets from Google Earth Engine. *Remote Sens.* **2021**, *13*, 453. [CrossRef]
87. Graesser, J.; Ramankutty, N. Detection of cropland field parcels from Landsat imagery. *Remote Sens. Environ.* **2017**, *201*, 165–180. [CrossRef]
88. Waldner, F.; Diakogiannis, F.I. Deep learning on edge: Extracting field boundaries from satellite images with a convolutional neural network. *Remote Sens. Environ.* **2020**, *245*, 111741. [CrossRef]
89. Achanta, R.; Susstrunk, S. Superpixels and polygons using simple non-iterative clustering. In Proceedings of the IEEE Conference on Computer Vision and Pattern Recognition, Honolulu, HI, USA, 21–26 July 2017; pp. 4651–4660. [CrossRef]
90. Schultz, B.; Immitzer, M.; Formaggio, A.R.; Sanches, I.D.A.; Luiz, A.J.B.; Atzberger, C. Self-guided segmentation and classification of multi-temporal Landsat 8 images for crop type mapping in Southeastern Brazil. *Remote Sens.* **2015**, *7*, 14482–14508. [CrossRef]
91. Xu, Q.; Fu, P.; Sun, Q.; Wang, T. A Fast Region Growing Based Superpixel Segmentation for Hyperspectral Image Classification. In Proceedings of the Chinese Conference on Pattern Recognition and Computer Vision (PRCV), Xi'an, China, 8–11 November 2019; Springer: Cham, Switzerland, 2019; pp. 772–782. [CrossRef]
92. Tassi, A.; Vizzari, M. Object-Oriented LULC Classification in Google Earth Engine Combining SNIC, GLCM, and Machine Learning Algorithms. *Remote Sens.* **2020**, *12*, 3776. [CrossRef]
93. Tu, Y.; Chen, B.; Zhang, T.; Xu, B. Regional Mapping of Essential Urban Land Use Categories in China: A Segmentation-Based Approach. *Remote Sens.* **2020**, *12*, 1058. [CrossRef]
94. Jia, S.; Zhan, Z.; Zhang, M.; Xu, M.; Huang, Q.; Zhou, J.; Jia, X. Multiple Feature-Based Superpixel-Level Decision Fusion for Hyperspectral and LiDAR Data Classification. *IEEE Trans. Geosci. Remote Sens.* **2020**, *99*, 1–19. [CrossRef]
95. Paludo, A.; Becker, W.R.; Richetti, J.; Silva, L.C.D.A.; Johann, J.A. Mapping summer soybean and corn with remote sensing on Google Earth Engine cloud computing in Parana state–Brazil. *Int. J. Digit. Earth* **2020**, *13*, 1624–2636. [CrossRef]
96. Brinkhoff, J.; Vardanega, J.; Robson, A.J. Land Cover Classification of Nine Perennial Crops Using Sentinel-1 and -2 Data. *Remote Sens.* **2020**, *12*, 96. [CrossRef]

97. Amani, M.; Mahdavi, S.; Afshar, M.; Brisco, B.; Huang, W.; Mohammad Javad Mirzadeh, S.; White, L.; Banks, S.; Montgomery, J.; Hopkinson, C. Canadian wetland inventory using Google Earth engine: The first map and preliminary results. *Remote Sens.* **2019**, *11*, 842. [CrossRef]
98. Verde, N.; Kokkoris, I.P.; Georgiadis, C.; Kaimaris, D.; Dimopoulos, P.; Mitsopoulos, I.; Mallinis, G. National Scale Land Cover Classification for Ecosystem Services Mapping and Assessment, Using Multitemporal Copernicus EO Data and Google Earth Engine. *Remote Sens.* **2020**, *12*, 3303. [CrossRef]
99. Shafizadeh-Moghadam, H.; Khazaei, M.; Alavipanah, S.K.; Weng, Q. Google Earth Engine for large-scale land use and land cover mapping: An object-based classification approach using spectral, textural and topographical factors. *GIScience Remote Sens.* **2021**, *58*, 914–928. [CrossRef]
100. Fahim, A.M.; Salem, A.M.; Torkey, F.A. An efficient enhanced k-means clustering algorithm. *J. Zhejiang Univ. Sci. A* **2006**, *10*, 1626–1633. [CrossRef]
101. Abdul Nazeer, K.A.; Sebastian, M.P. Improving the Accuracy and Efficiency of the k-means Clustering Algorithm. In Proceedings of the World Congress on Engineering 2009, London, UK, 1–3 July 2009; Volume 1. Available online: https://www.researchgate.net/publication/44260003_Improving_the_Accuracy_and_Efficiency_of_the_k-means_Clustering_Algorithm (accessed on 1 September 2024).
102. Romahn, F.; Pedergnana, M.; Loyola, D.; Apituley, A.; Sneep, M.; Veefkind, J.P. *S5P/TROPOMI L2 Product User Manual Sulphur Dioxide SO_2—S5P-L2-DLR-PUM-400E*; European Space Agency: Paris, France, 2022.
103. Valade, S.; Ley, A.; Massimetti, F.; D'Hondt, O.; Laiolo, M.; Coppola, D.; Loibl, D.; Hellwich, O.; Walter, T.R. Towards global volcano monitoring using multisensor Sentinel missions and artificial intelligence: The MOUNTS monitoring system. *Remote Sens.* **2019**, *11*, 1528. [CrossRef]
104. Branca, S.; Del Carlo, P. Eruptions of Mt Etna during the past 3,200 years: A revised compilation integrating the historical and stratigraphic records. *Geoph. Monog. Ser.* **2004**, *143*, 1–27. [CrossRef]
105. Branca, S.; Del Carlo, P. Types of eruptions of Etna volcano AD 1670–2003: Implications for short-term eruptive behavior. *Bull. Volcanol.* **2005**, *67*, 732–742. [CrossRef]
106. Andronico, D.; Lodato, L. Effusive Activity at Mount Etna Volcano (Italy) During the 20th Century: A Contribution to Volcanic Hazard Assessment. *Nat. Hazards* **2005**, *36*, 407–443. [CrossRef]
107. Branca, S.; Coltelli, M.; Groppelli, G. Geological evolution of a complex basaltic stratovolcano: Mount Etna, Italy. *Ital. J. Geosci.* **2011**, *130*, 306–317. [CrossRef]
108. Andronico, D.; Cannata, A.; Di Grazia, G.; Ferrari, F. The 1986–2021 paroxysmal episodes at the summit craters of Mt. Etna: Insights into volcano dynamics and hazard. *Earth-Sci. Rev.* **2021**, *220*, 103686. [CrossRef]
109. Monzier, M.; Robin, C.; Samaniego, P.; Hall, M.L.; Cotten, J.; Mothes, P.; Arnaud, N. Sangay volcano, Ecuador: Structural development, present activity and petrology. *J. Volcanol. Geotherm. Res.* **1999**, *90*, 49–79. [CrossRef]
110. Hall, S.R.; Farber, D.; Audin, L.; Finkel, R.; Mériaux, A.-S. Geochronology of pediment surfaces in southern Peru: Implications for Quaternary deformation of the Andean forearc. *Tectonophysics* **2008**, *459*, 186–205. [CrossRef]
111. Jing, F.; Chauhan, A.; Singh, R.P.; Dash, P. Changes in atmospheric, meteorological, and ocean parameters associated with the 12 January 2020 Taal volcanic eruption. *Remote Sens.* **2020**, *12*, 1072. [CrossRef]
112. Salerno, G.G.; Burton, M.R.; Oppenheimer, C.; Caltabiano, T.; Tsanev, V.; Bruno, N. Novel retrieval of volcanic SO_2 abundance from ultraviolet spectra. *J. Volcanol. Geotherm. Res.* **2009**, *181*, 141–153. [CrossRef]
113. Mallapaty, S. Scientists fear major volcanic eruption in the Philippines. *Nature* **2020**, *157*, 7791. [CrossRef]
114. Kazemi Garajeh, M. Monitoring the Spatio-Temporal Distribution of Soil Salinity Using Google Earth Engine for Detecting the Saline Areas Susceptible to Salt Storm Occurrence. *Pollutants* **2024**, *4*, 1–15. [CrossRef]
115. Fiantis, D.; Zulhakim, H.; Yulanda, N.; Ginting, F.I.; Gusnidar; Yasin, S. Tracing sulphur dioxide in volcanic deposits and ash emission during the 2019 Sinabung eruptions. In Proceedings of the IOP Conference Series: Earth and Environmental Science, Medan, Indonesia, 25–26 July 2024; Volume 1306, p. 012020. [CrossRef]